

To: Suresh Garimella

**Numerical Simulations of Crystal Growth of an Alloy
under Microgravity Conditions[§]**

*this is a
10/4/98 page Fax*

James E. Simpson, Suresh V. Garimella[†]
Department of Mechanical Engineering
University of Wisconsin-Milwaukee
P.O. Box 784, Milwaukee, Wisconsin 53201
Phone: (414) 229-6535; Fax: (414) 229-6958
email: sureshg@uwm.edu

① LOI

② B.L.S + Exp. Comp.

and Henry C. de Groh III
NASA Lewis Research Center
Cleveland, Ohio 44135

*Reya Abbasthion
U.S. @ G*

1999202482

ABSTRACT

The directional solidification of a dilute binary alloy (Bi-1.0 at.% Sn) is investigated. Results are obtained at a gravity level of 1 μ g. Computations are performed in two dimensions with a fixed, non-uniform grid. The simulation involves a solution of the species concentration equation (modified to account for solute rejection at the interface) and energy equation (modified to account for phase-change) for both the solid and liquid phases, in addition to the constitutive equations for describing convective flow in the melt. The effects of conductive heat transfer in the ampoule and in a capillary tube in the sample are included. To gauge the effects of including this growth capillary tube in the apparatus, simulations both with and without the capillary tube are presented and compared. Fully transient simulations have been performed; no simplifying steady-state approximations are used. *however, the influence of solute on the melting temp at the interface is not included* Both thermal and solutal convective cells are seen to form. Convective velocities are significantly damped ~~for melt~~ inside the capillary, causing less segregation due to convection. As solidification proceeds beyond the capillary tube, longitudinal segregation arises as a result of the change in cross-sectional area of solidifying material. The magnitudes of the velocities in this cell increase significantly once the solid/liquid front passes beyond the end of the capillary tube; this causes a corresponding increase in the level of radial solute segregation in the solidified material.

[§]Submitted for possible presentation at ASME National Heat Transfer Conference, Albuquerque, New Mexico, August 1999.

[†]Cray-Research Associate Professor, *author to whom correspondence should be addressed*

NOMENCLATURE

A	area
c_p	specific heat at constant pressure
C	species concentration
D	species diffusion coefficient
E	energy
f	volume fraction
g	acceleration due to gravity
Gr	Grashof number, $g\beta_T(T_H - T_C)H^3/\nu^2$
Gr_s	solutal Grashof number, $g\beta_c C_0 H^3/\nu^2$
h	ampoule thickness (outside radius - inside radius)
H	ampoule diameter; reference length
k	thermal conductivity
k_p	segregation coefficient
L	length of simulation domain
L_A	translating zone length
Le	Lewis number, α/D
Pr	Prandtl number, ν/α
rhs_{ij}	coefficient matrix in equation (10)
RHS_{ij}	coefficient matrix in equation (7)
t	time
T	temperature
u,v,w	velocities in the x, y, z directions

Greek Symbols

α	thermal diffusivity
β	expansion coefficient
ΔT	temperature difference, $T_H - T_C$
ΔH	enthalpy of freezing
ϵ	temperature difference for phase-change in equation (8)
θ	nondimensional temperature, $(T - T_C)/(T_H - T_C)$

Γ_{ij} coefficient matrix in equation (7)
 Λ_{ij} coefficient matrix in equation (10)
 μ dynamic viscosity
 ξ radial segregation, $(C_{\max} - C_{\min})/C_{\text{average}}$
 ρ density
 ψ stream function (z component of vector potential)

Subscripts

0 initial condition
 C cold furnace temperature condition
 H hot furnace temperature condition
 i, j located at i, j th finite volume center
 I, J located at I, J th finite difference mesh point
 L liquid
 m at solidification front
 S solid
 w ampoule wall

Superscripts

\wedge unit vector
 \sim vector
 $*$ reference quantity
 n time step n
 p iteration count p

INTRODUCTION

Increased demands on the performance of military, industrial and home electronics have created the need for semiconductor materials of higher quality. Semiconductors are deleteriously influenced by the presence of compositional non-uniformities and crystal lattice defects. The primary mechanism which causes the formation of these defects is gravity-induced convection. The low-gravity environment of Space offers an opportunity to suppress ~~the strength of~~ this natural convection. Hence there is a great deal of interest in the study of the synthesis of crystals in Space.

The MEPHISTO project (Abbaschian et al., 1992) is a collaborative program of space experiments aimed at understanding the fundamental processes involved in crystal growth. The Space-borne experimental apparatus is a Bridgman-type furnace with an isothermal hot zone, an isothermal chill zone, and an insulated gradient zone. The furnace contains three ingots of Bi-Sn alloy inside fused silica ampoules with a maximum 6 mm inner diameter and a 10 mm outer diameter. All three samples are solidified simultaneously, under identical thermal conditions. After flight, the samples are extracted and subjected to post-flight analysis. The most recent experiment, MEPHISTO-4, was flown in November 1997. Modifications to the experimental apparatus undertaken for this flight included the addition of a 2 mm inner diameter capillary tube that extends half-way through the process zone.

The MEPHISTO project also includes a program of computational modeling of the crystal growth process. In particular, the role of convection, which is crucial to a complete understanding of the process, is to be investigated. Since accurate experimental determination of convection in metallic melts is very difficult to achieve due to the opacity and chemical reactivity of the melts, convective levels are determined numerically (Abbaschian, 1996).

Many simulations of Bridgman crystal growth ~~processes~~, both under terrestrial and

microgravity conditions, are available in the literature. The majority of these simulations can be classified as *pseudo steady state* models. The key assumption in such models is that a “steady state” mode of alloy solidification exists, i.e. the concentration of the dopant in the solid which forms at the interface is equal to the initial dopant concentration in the liquid (Kurz and Fisher, 1989). Such models vary in complexity from simple 2D analyses that consider the interface to be flat (Alexander et al., 1989; Yao et al., 1995; Simpson et al., 1998a) to much more complex formulations that are able to handle interface curvature and wall conduction (Adornato and Brown, 1987) and fully three dimensional simulations (Liang and Lan, 1996). However, because of the low partition coefficient for Bi-Sn alloys, a steady-state mode of solidification is never achieved during the MEPHISTO experiments. Thus pseudo steady state models are not appropriate; recently developed fully transient simulations, such as those of Simpson et al. (1998b) and Timchenko et al. (1998) need to be employed and improved in order to faithfully model this process.

Convection effects at microgravity levels (10 μ g) and the influence of the 2 mm diameter growth capillary have been modeled by means of a transient, 2D FIDAP finite-element model (Yao et al., 1997). A fixed-grid approach was used, with the enthalpy method being employed to model the phase change. Temporal averaging was used for the apparent heat capacity in the discretized equations. While this work furnished useful information about interface curvature and convective levels, the simulation did not include the presence of a solute (due to numerical difficulties arising from the small partition coefficient for Bi-Sn alloys, pure Bi was considered). As a result, many effects such as segregation in the solidified material and the impact of the capillary on the melt solute fields could not be quantified.

The computational modeling presented in this paper is intended to examine the effects of thermosolutal natural convection and the inclusion of a capillary tube on the MEPHISTO-4

solidification experiments. Both radial and axial segregation in the solidified material will be quantified. This will be achieved using a fully transient 2D model, which includes most of the effects of binary alloy solidification, convection driven by both thermal and solutal gradients, distinct thermal properties in the solid and liquid phases, and the effects of interface curvature. The solution scheme used in this work, compared to that used in Simpson et al. (1998b), is improved as discussed in the following section. Conduction through the ampoule and capillary tube walls (both of which are made of fused silica) will be considered, while the dependence of melting temperature on concentration will be ignored. For the purposes of our model, we assume that the liquid/solid interface remains distinct like that for a pure material.

↳ What does this mean? Flat? or at T_m for Pure Bi.?

MATHEMATICAL FORMULATION

The problem under consideration is the directional solidification of a binary alloy by the Bridgman process, as shown schematically in Fig. 1. The gravity vector is perpendicular to the furnace axis (horizontal Bridgman growth configuration). The melt region is considered to be a viscous Newtonian fluid subject to thermosolutal convection. Thermophysical properties are considered as constant but distinct for the solid and liquid phases. Density variations are considered to be subject to the Boussinesq approximation. The governing equations for the velocity field in terms of vorticity and vector potential, as well as the boundary conditions employed, are discussed in detail in Simpson and Garimella (1998) and are not repeated here. In the nondimensionalizations used, the ampoule inside diameter H is selected to be the reference length. The characteristic time and velocity become $t^* (= H^2/\alpha)$ and $v^* (= H/t^* = \alpha/H)$.

The governing equation for the conservation of energy is

$$A(T,C) \frac{\partial T}{\partial t} + \rho c_p L \nabla \cdot (\bar{u} \theta) = \nabla \cdot (k \nabla T) + B(T,C) \quad (1)$$

It will be seen below that effective heat capacity A and source term B may be specified in this way for calculating phase-change. An initial temperature equal to T_H is applied throughout the flow field. The temperatures at the $x = 0$ and $x = L$ walls are set to be T_H and T_C , respectively.

The thermal boundary conditions along $y = \pm (H/2 + h)$ required for the Bridgman process need closer examination, since they are a function of time. A schematic of the temperature imposed at these boundaries, which approximates the furnace, is shown in Fig. 1. There is a translating zone (considered an “adiabatic” zone if the temperature profile is unknown) between the hot and cold regions of the furnace, in which the temperature linearly increases from the cold furnace temperature to the hot furnace temperature. The melting temperature of the material occurs somewhere within this zone, which translates with time at a constant x -velocity, known as the *translation velocity*, u_t . This is what facilitates the directional growth of the crystal. Defining the x location where the translating zone meets the cold furnace temperature zone to be at $x_A(t)$, the boundary condition for temperature may be expressed as

$$\text{at } y = \pm \left(\frac{H}{2} + h\right): \quad T = \begin{cases} T_C, & \text{for } x < x_A(t) \\ T_C + \Delta T \frac{x - x_A(t)}{L_A}, & \text{for } x_A(t) \leq x \leq [x_A(t) + L_A] \\ T_H, & \text{for } x_A(t) < x \end{cases} \quad (2)$$

In principle, the solution of the energy equation (1) coupled with the solution of the vorticity-vector potential equations would yield the temperature and velocity distribution throughout the simulation domain. However, the problem of modeling the physics of the propagation of the solidification front and determining its location remains to be addressed. We choose to do this by employing the phase-transformation model of Zeng and Faghri (1994). For the present study, concentration-dependence

on temperature is neglected; terms A and B may be written as

$$\begin{aligned}
A(T) &= \rho(c_{pL}f_L + c_{pS}f_S) + a(T)\frac{\partial f_L}{\partial T} \\
B(T) &= 0 \\
a(T) &= \rho[(c_{pL} - c_{pS})T + \Delta H]
\end{aligned} \tag{3}$$

The equation for conservation of solute throughout the computational domain is

$$\frac{\partial C_L}{\partial t} + \nabla \cdot (\bar{u} C_L) = D \nabla^2 C_L + S(T, C_L) \tag{4}$$

This equation is analogous to the energy equation. We impose an initial solute concentration throughout the solution domain. At the boundaries no solute may exit the domain. Thus,

$$\begin{aligned}
t = 0 & \quad C_L = C_0 \\
x = 0, L & \quad \partial C_L / \partial x = 0 \\
y = 0, H & \quad \partial C_L / \partial y = 0
\end{aligned} \tag{5}$$

Again, in principle, solution of equation (4) along with energy equation (1) and the vorticity-vector potential equations all subject to the relevant boundary and initial conditions is enough to determine the solute, temperature and velocity values throughout the solution domain. However, the more general problem involving phase change demands that the thermodynamics of solute redistribution be addressed. Following the work of Swaminathan and Voller (1997) and Voller et al. (1989), these effects may be handled by source term S which is the differential

$$S(T, C) = \frac{\partial (f_L C_L)}{\partial t} + k_p C_L \frac{\partial f_S}{\partial t} \tag{6}$$

NUMERICAL ANALYSIS

The computational domain is primarily discretized using regularly spaced finite difference mesh points. Superimposed on this grid are finite volumes which are used for the solution of the

energy and species concentration equations. The finite volume centers are staggered with respect to the finite difference mesh point locations. The finite volumes in the ampoule have a different size than those in the bulk of the domain; hence this mesh is non-uniform. Vorticity, velocity and vector potential are calculated at the finite difference mesh points. Temperature and solute concentration are evaluated at the finite volume centers as a result of the solution of equations (1) and (4).

A brief description of the numerical algorithm for the solution of the vorticity and vector potential equations is as follows. The approach used here is modified from a program (Timchenko et al., 1997) written for the solution of natural convection in a rectangular cavity. The essential details are that the equations for vorticity transport and vector potential are discretized in space using the regular finite difference mesh. The discretized equation for vorticity transport is solved using an Alternating Direction Implicit (ADI) scheme (Samarskii and Andreyev, 1963). The discretized equation for vector potential is solved using the conjugate gradient method. This is a semi-iterative method used to solve specific systems of linear equations. The method is not discussed here, except to note that the values for vector potential at the previous time step are used as the initial guess values. Once the values of vector potential are known, the nodal velocities can be determined. Further details on the solution scheme for vorticity and vector potential and the manner in which the algorithm handles boundary conditions at the arbitrarily oriented interface may be found in Simpson and Garimella (1998).

An outline of the solution scheme for the energy equation (1) is as follows. The energy equation is discretized using the finite volume mesh, with an upwind scheme incorporated for the treatment of convective heat fluxes. A complete methodology for the solution of similar discretized equations including the modifications required to account for the presence of the ampoule wall and capillary tube is provided in Simpson and Garimella (1997) and Garimella and Simpson (1998). The

discretized equation is advanced forward in time using Gauss-Seidel iteration with successive over relaxation. For this method, we may write

$$\left[1 + \Gamma_{i,j}^p\right] T_{i,j}^{p+1} = \text{RHS}_{i,j}^p \quad (7)$$

in which p denotes the inner iteration number and the RHS matrix is fully explicit at iteration p . The values at time step n are used as the first approximation. Iterations proceed until convergence, at which time the new values at time step $n+1$ for temperature are declared to be those found at convergence. Convergence is assessed by examining the change in the solution and in the solution residual with a tolerance of 10^{-6} (Barrett et al., 1994; Garimella and Simpson, 1998). In cells which contain the interface, the cell liquid fractions may be found using the volume fraction-temperature relation

$$f_L = \begin{cases} 0, & \text{for } T < T_m - \varepsilon \\ T_C + \frac{1}{2\varepsilon} (T - T_m + \varepsilon), & \text{for } T_m - \varepsilon \leq T \leq T_m + \varepsilon \\ 1, & \text{for } T > T_m + \varepsilon \end{cases} \quad (8)$$

Numerical experiments have shown results to be optimal when temperature 2ε is selected such that no more than two finite volumes undergo phase change at any given time. The specification of liquid volume fraction allows the front orientation, needed for the calculation of vorticity at the interface, to be determined using the approach of Hirt and Nichols (1981).

The assumptions made in formulating the discrete form of the species concentration equation (and source term S in Eq. 6) are that the densities of the liquid and solid phases are constant and equal, so that a simple mixture rule applies, and that there is no diffusion in the solid (except in the cells that contain the interface, in which the equilibrium lever rule is assumed); the concentration at which the solute first solidifies is the concentration at which that portion of solid remains for all time.

→? volume, or liquid, or solid, or solvent?

Solution of this finite volume equation is explained in Simpson and Garimella (1998). For the purposes of our model, we assume that there is no effect of concentration on the melting temperature and the liquid/solid interface remains distinct like that for a pure material. The significant result of this assumption is that the energy equation is decoupled from the concentration equation and is the only mechanism necessary to determine the location of the solidification front. However, the method may be easily generalized to couple the concentration and energy equations more closely by incorporating a concentration-dependent melting temperature (Zeng and Faghri, 1994).

The solute concentration in the solid portion of a node may be found from employing the relation

$$C_s^{n+1} = \frac{C_s^n f_s^n + k_p C_L^n (f_L^{n+1} - f_L^n)}{f_s^{n+1}} \quad (9)$$

The discretized equation is solved by Gauss-Seidel iteration in a manner analogous to the energy equation, i.e.,

$$\left[1 + \Lambda_{i,j}^p\right] C_{L,i,j}^{p+1} = \text{rhs}_{i,j}^p \quad (10)$$

The solution scheme for fully transient solidification in two-dimensional Bridgman crystal growth subject to thermosolutal convection has now been specified.

RESULTS AND DISCUSSION

Simulations for the Bridgman crystal growth of a Bi-1.0 at.% Sn alloy were performed. In order to fully examine the influence of the capillary tube on the growth process, solidification both with and without the capillary tube was considered. Thermophysical properties (for pure bismuth)

For future simulations we should check this.
 The Furnace Temp. we used during flight can be checked on the CP.

from Yao et al. (1995) were employed. The cold and hot furnace temperatures were $T_c = 50^\circ\text{C}$ and $T_H = 700^\circ\text{C}$ respectively. The liquid composition was taken to be at a uniform value of 1.0 at.% Sn (0.8185 vol.% Sn) as the initial condition. Liquid properties were used as the reference properties in the nondimensionalization. The properties were evaluated at the mean solid and the mean liquid temperatures of 160.7 and 485.7°C , respectively. The reference density was considered to be equal for both phases. The property values were: $k_s = 6.872\text{ W/mK}$, $k_L = 14.66\text{ W/mK}$, $\rho_0 = 10,070\text{ kg/m}^3$, $c_{pS} = 132.6\text{ J/kgK}$, $c_{pL} = 135.3\text{ J/kgK}$, $\Delta H = 52.3\text{ kJ/kg}$, $\mu = 1.240 \times 10^{-3}\text{ Ns/m}$ and $T_m = 271.3^\circ\text{C}$. The thermal and solutal expansivities of the liquid were taken to be $\beta_T = -1.25 \times 10^{-4}\text{ K}^{-1}$ and $\beta_C = -0.305\text{ (vol.\%)}^{-1}$, respectively. In addition, the value for diffusivity of liquid Sn in liquid Bi was $D = 3.50 \times 10^{-9}\text{ m}^2/\text{s}$, and the partition coefficient was $k_p = 0.029$. The properties used for the fused silica ampoule wall and capillary tube were $k_w = 2.10\text{ W/mK}$, $\rho_w = 2,020\text{ kg/m}^3$, $c_{pw} = 1066.8\text{ J/kgK}$. The dimensions used to define the domain were $H = 6\text{ mm}$, $L = 75\text{ mm}$ and $h = 2\text{ mm}$. The length of the insulated translating zone was $L_A = 25\text{ mm}$, with a translation velocity of $u_t = 3.38\text{ }\mu\text{m/s}$. The capillary tube has an inner diameter of 2 mm, in inner diameter with 0.5 mm thick wall, and is 35 mm long. A gravity level of $1\text{ }\mu\text{g}$, with gravity acting in the negative y direction was used; this is the expected steady gravity level and direction encountered during Space experiments (de Groh and Nelson, 1994). Key nondimensional quantities derived from these properties and conditions are $\text{Gr} = 11.36$, $\text{Gr}_s = 0.3490$, $\text{Pr} = 0.01144$ and $\text{Le} = 3074$.

No capillary

For the simulation without the capillary, the computational domain was discretized in the following manner. A 300×35 mesh was used, with 25 of the 35 y-direction cells occupying the sample and the remaining 10 cells being in the ampoule walls. This mesh scheme was selected as

a result of numerical experiments which indicated its adequacy in resolving solute gradients in the liquid near the interface. The temporal step size was $\Delta t = 0.1338$ s. In order to start the crystal growth simulations, the following procedure was used in each case. The initial position of the *cool end of the* translating zone was flush with the $x = 0$ wall. This zone was immobilized for the first 3,000 time steps. During this time, the velocity and concentration field solution schemes were switched off while solid rapidly chilled in the portion of the translating zone which was lower in temperature than T_m . This new state was then taken to be at time $t = 0$. After this, simulations proceeded with the entire solution scheme enabled and the insulated zone moving at the translation velocity u_t .

Velocity vectors and isotherms after 3,000, 6,000 and 9,000 s for this alloy are shown in Fig.

2. The velocity vectors in Fig. 2 (a) indicate a primary convective cell rotating in a counter-clockwise manner in the translating zone, along with a weak secondary, clockwise convective cell driven by solute gradients adjacent to the interface. Solute rejection at the interface leading to the formation of a solute boundary layer is responsible for the formation of the secondary cell. This two-cell convective motion is in stark contrast to the single-cell convective motions observed for pure materials and more dilute alloys (Simpson et al., 1998b). The maximum v-velocity in the secondary convective cell near the interface at (16.5, 0 mm) is $0.05859 \mu\text{m/s}$. The highest velocity in the domain is found in the thermally-driven cell, giving a maximum u-velocity of $0.3794 \mu\text{m/s}$ at (25.5, -1.8 mm). The maximum v-velocity magnitude is $-0.1866 \mu\text{m/s}$ acting downward at (19.25, 0 mm). These values show that velocities in the thermally driven convective cell are much higher than those found in the secondary cell at this time. At a later time (6,000 s), the front is at $x \approx 26$ mm, as shown in Fig. 2 (b). The secondary convective cell has increased in size and strength as solute – the driving force for this cell – continues to build up at the interface. The maximum v-velocity in the secondary convective cell near the interface at (27.00, 0.12 mm) is $0.1794 \mu\text{m/s}$ (note that this location is

This is a lot, longer than you need to, though valuable and interesting. Solidification dist. in the space exp. were usually $\leq 10^{-1}$

slightly above the centerline) and the maximum u-velocity in the domain has decreased to $0.3434 \mu\text{m/s}$ at $(36.00, -1.8 \text{ mm})$. Later in the growth process (9,000 s, Fig. 2 (c)), the front has advanced to $x \approx 36 \text{ mm}$, and the secondary convective cell has become quite strong. The maximum u-velocity in the domain is $0.3427 \mu\text{m/s}$ at $(46.25, -1.8 \text{ mm})$, while the maximum v-velocity in the secondary cell (and in the domain) is $0.3125 \mu\text{m/s}$ at $(37.00, 0.12 \text{ mm})$. Since the magnitude of the velocities in all cases is small ($< 1 \mu\text{m/s}$), we anticipate that there will be only a minimal impact of convection on solute segregation.

Traces of solute concentration across the height of the solidified alloy in the domain are shown in Fig. 3. Three different x-locations (16.18, 26.30, 36.41 mm) are considered; these locations correspond to the location of the interface at $y = 0$ at times of 3,000, 6,000 and 9,000 s, respectively. To aid in visualizing the influence of convection, results for a simulation involving diffusion only (no convection) are superimposed on this plot (dotted lines). Note that these pure diffusion results indicate that significant radial segregation arises due to interface curvature (Adornato and Brown, 1987; Liang and Lan, 1996) such that the values for solute concentration at the centerline are larger than those at the edges. The level of curvature-induced radial segregation remains almost constant, with values of $\xi = 29.1\%$ (based on the mean concentration) at $x = 16.18 \text{ mm}$ and 29.4% at $x = 26.30$ and 36.41 mm . The inclusion of convection into the calculations causes the following effects. The formation and growth of the secondary cell causes additional, convection-based segregation to occur such that concentration values near the top of the domain are higher than those at the bottom. For the trace at $x = 16.18 \text{ mm}$, the concentration values are close to the values predicted from the pure diffusion analysis; the maximum value is $C_{\text{max}}/C_0 = 0.2833$ at $y = 0.0 \text{ mm}$ with a segregation value of $\xi = 29.5\%$. This serendipitous result is a consequence of the segregation arising from the influence of the secondary cell balancing that caused by the thermally driven cell

when solidification has proceeded to this location. At lower values of x ($t < 3,000$ s), segregation is such that the maximum value occurs at $y < 0$ while at higher values of x ($t > 3,000$ s) this maximum is shifted to a ~~more~~ positive y value. The traces at $x = 26.30$ and 36.41 mm show that increasing solutal convection leads to increasing radial segregation, and a shift away from the centerline in the location of maximum concentration; The maximum values are $C_{\max}/C_0 = 0.4745$ ($y = 0.1763$ mm) and 0.6208 ($y = 0.4114$ mm) with radial segregation levels of $\xi = 32.1$ and 34.4% , respectively. Thus, the levels of radial segregation are slightly increased over the values found for the pure diffusion case, and the level of convection-induced segregation increases with increasing time. *after 3000s.*

Figure 4 is a plot of longitudinal solute traces at domain heights of $y = -2.88, 0$ and 2.88 mm for times of $3,000, 6,000$ and $9,000$ s. Solute concentrations in *both* the liquid and solid are shown. There is significant solute buildup, with values of liquid solute concentration C/C_0 at the interface along the centerline being $9.78, 16.3$ and 21.3 , respectively. Values for solute in the solid are slightly higher for the $y = 2.88$ mm trace than that for $y = -2.88$ mm at later times. Had convection not been included in the simulation, these traces would have been identical. In the liquid near the interface, the concentration profiles for the $y = 2.88$ mm trace are also slightly higher than those found for the $y = -2.88$ mm trace; however this effect is small and difficult to discern from the plot. At $9,000$ s, the liquid solute concentration values at the interface are $C/C_0 = 16.7$ and 14.8 at $y = 2.88$ mm and -2.88 mm, respectively. *Figures 3 and 4* This plot shows that convection has had only a minor effect on the solute profiles. Note that concentration values of the magnitudes indicated would be sufficient *(about 20 to 40 K)* to lower the melting temperature of the alloy by a significant amount (Simpson et al., 1998a). This implies that the constant melting temperature assumption is not valid. The likely effect of concentration-dependent melting temperature would be to increase the level of interface curvature! *about 1 to 2 mm*

Why this plot? No diffusion only comparison is provided.

$\Delta C = 10$
 $\Delta T \approx 23 K$

$\Delta C = 10$
 $\Delta T \approx 21 K$

This will be addressed in future work.

Capillary included

For the simulation with the capillary, a 300×46 mesh is used. Extra nodes are required in the y-direction in order to resolve velocities inside the capillary, with 36 of the 46 y-direction cells being contained within the sample (and capillary) and the remaining 10 cells spanning the ampoule walls. The temporal step size was decreased to $\Delta t = 0.06452$ s due to the smaller cell size. The initial condition was attained by the same procedure as outlined above for the no-capillary case. After this, simulations proceed with the entire solution scheme enabled and the insulated zone moving at the translation velocity u_r .

Plots of velocity vectors and isotherms are presented in Figure 5. Figure 5 (a) is at a time of $t = 3,000$ s. There are several interesting features depicted in this plot. The capillary walls are seen to extend into the computational domain to $x = 35$ mm. Heat transfer through the capillary is considered, but the capillary wall is otherwise impermeable to the melt and represents a no-slip/no-penetration boundary. The shapes of the isotherms are discernibly different from those depicted in Fig. 2 (a). In the ampoule and in the melt outside the capillary tube, the isotherms have a similar shape. However, the presence of the low-conductivity fused silica capillary tube distorts the isotherms. A higher temperature difference is required across the tube in order to maintain the radial heat transfer rate mandated by the thermal boundary condition. The thick solid line is an isotherm at the melting temperature of the alloy and thus represents the ^{approximate} location of the solid/liquid interface. As with the other isotherms, its shape has been distorted by the influence of the capillary. This causes the interface location inside the capillary to be offset with respect to that outside the capillary. The impact of this difference in interface location on solute levels in the solid will be expanded upon

TM is difficult to read and is not stressing what is important - that being the velocities near the interface inside and outside the capillary.

later. As would be expected, the presence of the capillary has led to a significant alteration to the velocity field. Outside the "capillary zone" ($x > 35$ mm), there is a large, thermally driven convective cell. The largest convective velocities may be found in this region, with a maximum u -velocity of $0.1096 \mu\text{m/s}$ at (x, y, z) of $(38.75, -1.834 \text{ mm})$. *3000s* Note that this velocity is considerably lower than the value of $0.3794 \mu\text{m/s}$ found for the no-capillary case. *This is not important*

Inside the capillary, the ~~magnitudes of the convective velocities~~ ^{on} ~~are~~ ^{is} significantly damped; however, a qualitative description of the flow structure is similar to the no-capillary case. There is a thermally driven cell along the bulk of the capillary length, while solute rejection at the interface leads to the formation of a secondary cell. Unlike the no-capillary case, the magnitude ^s of the velocities in the thermally driven cell ($0.01418 \mu\text{m/s}$ at $x = 25.25$ mm, $y = -0.5$ mm) ^{are} ~~is~~ lower than those in the solutally driven cell ($0.02092 \mu\text{m/s}$ at $x = 17.25$ mm, $y = 0.667$ mm) at this time. The maximum v -velocity near the interface is $0.01610 \mu\text{m/s}$ at $(16.75, 0 \text{ mm})$. This value is 3.64 times smaller than for the no-capillary case. The reduction in convective velocities will yield lower levels of segregation due to convection; this is detailed in Fig. 6. The flow patterns in the region of flow outside the capillary are similar to those inside but with slightly lower flow magnitudes. *OK, I think the main issue is the solute cell*

Figure 5 (b) is a plot of velocities and temperatures after 6,000 s have elapsed. At this time, approximately half of the length of the translating zone (and therefore half of the applied temperature gradient) extends past the end of the capillary. Consequently, the large convective cell at $x > 35$ mm has increased in strength, with the maximum u -velocity increasing to $0.2922 \mu\text{m/s}$ at $(40, -1.834 \text{ mm})$. Increasing solute rejection at the interface has led to higher velocities in the cell driven by solutal gradients; the v -velocity has increased to $0.02969 \mu\text{m/s}$ at $(26.75, 0 \text{ mm})$. Note that this is 6.04 times smaller than for the no-capillary case (Fig. 2 (b)); the disparity in convective levels has

increased with time. Figure 5 (c) is a plot of velocity vectors and isotherms at $t = 9,000$ s. At this

The rate of solute rejection is constant.

*Q. Why is the capillary not dampening the flow more?
Gr $\propto L^3$ \therefore $V_{\text{outside}} = \frac{6^3}{2^3} = 27$ - I think. Now would be a good time V_{inside} reference $V_{\text{no capillary}}$ TM (w/ capillary).*

time, the solid/liquid front has progressed beyond the end of the capillary (which can just be seen at $x = 35$ mm in the figure). Since the capillary is embedded in the solid and can no longer influence the flow, the velocity and thermal fields for this case reduce to the no-capillary case (Fig. 2). The magnitude of the maximum velocity in the thermally driven cell is $0.3573 \mu\text{m/s}$ at $(46.25, -1.834 \text{ mm})$. As expected, this is similar to the value of $0.3427 \mu\text{m/s}$ for Fig. 2 (c). The maximum value for v -velocity near the interface has increased (by an order of magnitude) to $0.2665 \mu\text{m/s}$ with respect to the velocity field at 6,000 s.

Traces of solute concentration across the ~~height of the solidified alloy in the domain~~ ^{ingot or sample} are shown in Fig. 6. The same x -locations (16.18, 26.30, 36.41 mm) as in Fig. 3 are considered. To highlight the influence of convection, diffusion-only (no convection) results are again superimposed on this plot. Solute profiles across the sample at $x = 16.18$ and 26.30 mm are shown for solid inside as well as outside the capillary. Several interesting features of these two traces need to be explained. The traces for the pure diffusion case and the case considering convection are almost identical; the low convective velocities in the capillary (Figs. 5 (a) and (b)) have caused minimal convection-induced radial segregation; the level of radial segregation is dominated by interface-curvature effects. Also note that the presence of the capillary has significantly influenced the transport phenomena that cause curvature-induced radial segregation. For the solid inside the capillary, the total interface deflection is small (~ 0.1 mm) ^{\rightarrow compare this with the center 2 mm of the No capillary case.} and so the resulting segregation is low ($\xi = 4.2\%$ for pure diffusion results in both cases). The solid outside the capillary has a much higher total interface deflection (~ 0.4 mm) ^{\rightarrow but this is over 6 mm is it not?} and correspondingly higher radial segregation ($\xi = 18.0\%$ for pure diffusion). Also note that since no solute can pass through the capillary wall the values for solute concentration on the inside and outside of the capillary wall (e.g. at $x \approx 0.9$ and $x \approx 1.3$ mm) are discontinuous. This is in contrast to the traces shown in Fig. 3 where the traces are continuous since there is no capillary.

I think you are missing the point, consider only $x=16$ there is no influence of convection for either Fig 3 or Fig 6

Sum of the important differences in the Fig 6 - Fig 3 case is the asymmetrical effects - those are caused by convection.

On first glance, it may appear that for a given x -location, the average value for the solute inside the capillary is lower than that outside the capillary; this is not the case: the average values are almost

identical for both regions. For the trace beyond the capillary zone, at $x = 36.41$ mm, the results are similar in nature to those shown in Fig. 3. Convective levels are much stronger once the solidification front passes the end of the capillary (refer to Fig. 5 (c)) and, correspondingly, there is a higher level of solute segregation for this case ($\xi = 38.4\%$). Note that, on average, solute

concentrations in the solid at this location are lower than those for the corresponding case shown in

Fig. 3 ($C_{av}/C_0 = 0.4898$ versus 0.5582): this will be expanded upon below. The maximum values for

solute concentration (inside the capillary where appropriate) are $C_{max}/C_0 = 0.2609, 0.4305$ and 0.5559 for the traces at $x = 16.18, 26.30$ and 36.41 mm, respectively.

Figure 7 is a plot of longitudinal solute traces at domain heights of $y = -0.9168, 0$ and 0.9168 mm (i.e. along the edges and centerline of the domain inside the capillary) for times of 3,000, 6,000 and 9,000 s. Solute concentrations in both the liquid and solid are shown. Figure 7 (a) illustrates the significant solute buildup, with values of liquid solute concentration C/C_0 at the interface along the centerline being 9.17, 15.0 and 18.9, respectively. Note the similarity in values for the three different domain heights; the values at the centerline are slightly higher than those at the periphery but this is difficult to discern since the level of radial segregation across the solid inside the capillary is small (refer to Fig. 6). Figure 7 (b) is a magnified view of the region near the end of the capillary ($30 \leq x \leq 40$ mm). The radial segregation and the effect of convection (as detailed in Fig. 6) is more apparent in this view. The trace at the centerline is higher than those at the edges while the trace for $y = 0.9168$ is higher than that for $y = -0.9168$ mm since convection acts to push solute towards the "top" of the domain (refer to Fig. 5). However, the most interesting detail shown in this figure is the "dip" in solid solute concentrations in the region $34 \leq x \leq 35.2$ mm. This is due to the change in

But if you consider the center 2mm only? ... just outside the capillary

cross-sectional area into which solute build up occurs as the solidification front passes the capillary (Flemings et al. 1968; Flemings and Nereo, 1968). As the front approaches the end of the capillary, the solute boundary layer extends past the end of the capillary and begins to diffuse (and convect) into a solute-poor region with a larger cross-section. As a result, solute is more rapidly diffused away from the interface and so the material solidifies at lower concentration levels. Once the front passes the end of the interface, the solute boundary layer (eventually) re-establishes itself and the solute build-up begins anew, as can be seen from the traces.

Nice work.

CONCLUSIONS

A series of fully transient simulations of horizontal Bridgman crystal growth of a Bi-1.0 at. % Sn alloy in microgravity conditions have been performed, both with and without including the effects of a 2 mm capillary in the processing zone. Results for the simulation without the capillary indicate the development of complex convective phenomena. Initially, a single, thermally driven, counter-clockwise rotating cell is present. As time proceeds and ^{the lighter Sn} solute accumulates at the interface, a secondary, solute-driven clockwise rotating cell develops. The effect of this convective pattern is to increase the level of radial segregation in the solute at the interface (and hence in the solid). This segregation is such that the values toward the top of the domain are higher. Results for the simulation with a capillary in the domain indicate that the convective flow is significantly damped inside the capillary, leading to lower levels of convection-induced segregation. The presence of the capillary also has an impact on the solute levels in the solidified material. Radial segregation in the solid due to interface curvature is reduced due to the physical presence of the capillary. There is also an "area effect" as solidification proceeds towards the end of the capillary which results in a lowering of the average solute concentration levels in the solid. Further simulations of Bridgman crystal

interface curvature causes most of the segregation and is the only source²⁰ of segregation for $x < 16$ as far as I can tell from the paper.

- ① Due to radial heat flow.
- ② To complicate to explain in one line
- ③ Decrease $T_{(1,1)}$ and $T_{(1,2)}$

Why is the interface curved? Why does this cause segregation?
What might be done to eliminate the curvature and the segregation?

growth in microgravity, incorporating the effects of a concentration-dependent melting temperature and including the effects of “g-jitter,” are planned as future work.

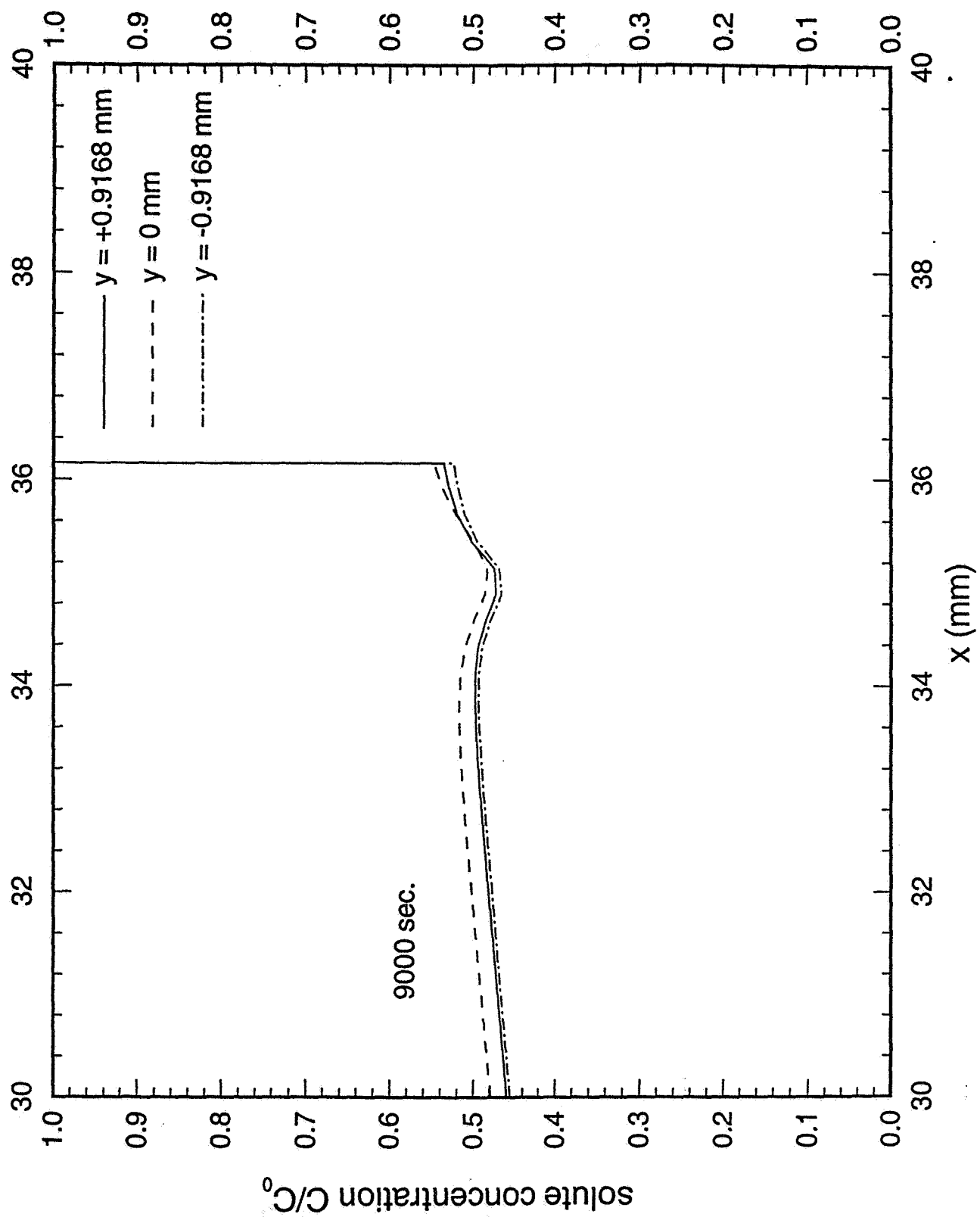
Acknowledgements

Partial funding for this work from NASA (Coop. Agreement # NCC3-600) is gratefully acknowledged. JES was funded by a UW-Milwaukee Graduate School Fellowship. ~~Professor Reza Abbaschian provided valuable guidance in the conduct of this work.~~ Professors G. de Vahl Davis and E. Leonardi and Dr. V. Timchenko of the University of New South Wales are thanked for kindly providing their code, FRECON3V, which was the starting point for this work.

REFERENCES

- Abbaschian, R., Gokhale, A. B., Favier, J. J. and Coriell, S. R., 1992, In-Situ Monitoring of Crystal Growth Using MEPHISTO, NASA Science Requirements Document (SRD).
- Abbaschian, R., 1996, In-Situ Monitoring of Crystal Growth Using MEPHISTO: Revised Science Requirements Document (RSRD) for the Re-flight of MEPHISTO aboard USMP-4.
- Adornato, P. M. and Brown, R. A., 1987, Convection and segregation in directional solidification of dilute and non-dilute binary alloys, *J. Crystal Growth*, Vol. 80, pp. 155-190.
- Alexander, J. I. D., Ouazzani, J. and Rosenberger, F., 1989, Analysis of the low gravity tolerance of Bridgman-Stockbarger crystal growth, *J. Crystal Growth*, Vol. 97, pp. 285-302.
- Barrett, R., Berry, M., Chan, T. F., Demmel, J., Donato, J. M., Dongarra, J., Eijkhout, V., Pozo, R., Romine, C. and Van der Vorst, H., 1994, *Templates for the Solution of Linear Systems: Building Blocks for Iterative Methods*, SIAM, Philadelphia.
- de Groh III, H. C. and Nelson, E. S., 1994, On residual acceleration during space experiments, *Heat Transfer in Microgravity Systems*, ASME HTD-Vol. 290, pp. 23-33.
- de Groh III, H. C. and Yao, M., 1994, Numerical and experimental study of transport phenomena in directional solidification of succinonitrile, *Transport Phenomena in Solidification*, ASME HTD-Vol 284, pp. 227-243.

- Flemings, M. C., Mehrabian, R. and Nereo, G. E., Macrosegregation, Part II, *Trans. AIME*, Vol. 242, pp. 41-49.
- Flemings, M. C. and Nereo, G. E., Macrosegregation, Part III, *Trans. AIME*, Vol. 242, pp. 50-55.
- Garimella, S.V. and Simpson, J. E., 1998, Interface propagation in the processing of metal matrix composites, *Microscale Thermophys. Eng.*, Vol. 2, pp. 173-188.
- Hirt, C. W. and Nichols, B. D., 1981, Volume of fluid (VOF) method for the dynamics of free boundaries, *J. Comp. Phys.*, Vol. 39, pp. 210-225.
- Kurz, W. and Fisher, D. J., 1989, *Fundamentals of Solidification*, Trans Tech Publications.
- Liang, M. C. and Lan, C. W., 1996, Three-dimensional convection and solute segregation in vertical Bridgman crystal growth, *J. Crystal Growth*, Vol. 167, pp. 320-332.
- Mallinson, G. D. and de Vahl Davis, G., 1973, The method of the false transient for the solution of coupled elliptic equations, *J. Comput. Phys.*, Vol. 12, pp. 435-461.
- Raw, W. Y. and Lee, S. L., 1991, Application of weighting function scheme on convection-conduction phase change problems, *Int. J. Heat Mass Transfer*, Vol. 34, pp. 1503-1513.
- Roache, P. J., 1976, *Computational Fluid Dynamics*, Hermosa.
- Samarskii, A. A. and Andreyev, V. B., 1963, On a high-accuracy difference scheme for an elliptic equation with several space variables, *USSR Comput. Math. and Math. Phys.*, Vol. 3, pp. 1373-1382.
- Simpson, J. E. and Garimella, S. V., 1997, Melt convection and front propagation in the unidirectional solidification of a pure material, *Procs. 4th Decennial Int. Conf. Solidification Processing*, Sheffield, UK, J. Beech and H. Jones (Eds.), pp. 130-134.
- Simpson, J. E. and Garimella, S. V., 1998, An investigation of the solutal, thermal and flow fields in unidirectional alloy solidification, *Int. J. Heat Mass Transfer*, Vol. 41, pp. 2485-2502.
- Simpson, J. E., Yao, M., de Groh III, H. C. and Garimella, S. V., 1998a, Numerical modeling of solidification in space with MEPHISTO-4 (Part 2), NASA Technical Memorandum TM-1998-206630.
- Simpson, J. E., Garimella, S. V., de Groh III, H. C. and Abbaschian, R., 1998b, Melt convection effects in the Bridgman crystal growth of an alloy under microgravity conditions, *Procs. 7th AIAA/ASME Jt. Thermophys. Heat Transfer Conf.*, ASME HTD-Vol. 357-4, pp. 123-132.
- Smith, V. G., Tiller, W. A. and Rutter, J. W., 1955, A mathematical analysis of solute redistribution during solidification, *Canadian J. Phys.*, Vol. 33, pp. 723-743.
- Timchenko, V., Chen, P. Y. P., de Vahl Davis, G. and Leonardi, E., 1998, Directional solidification



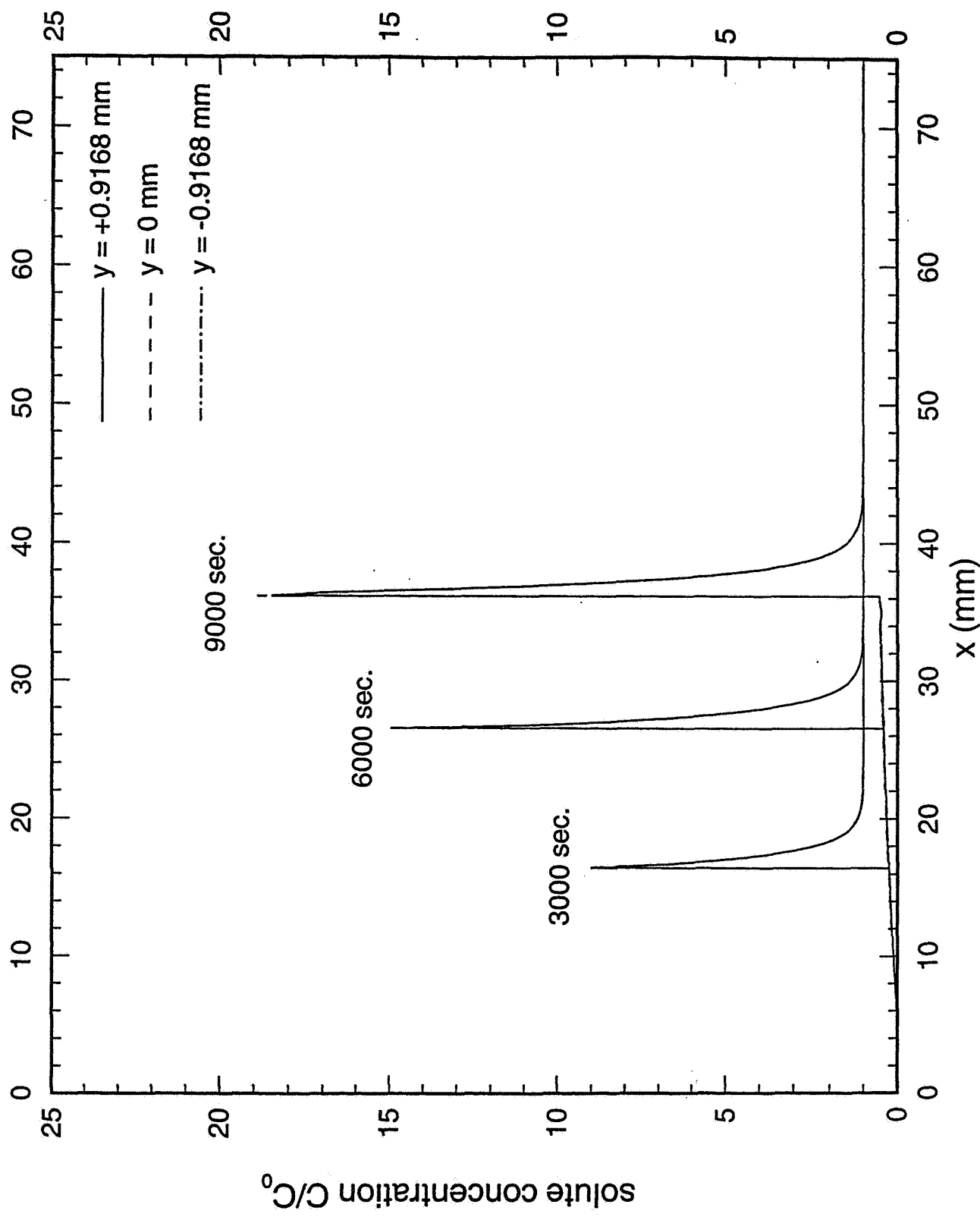


Figure 7(a), Simpson et al.

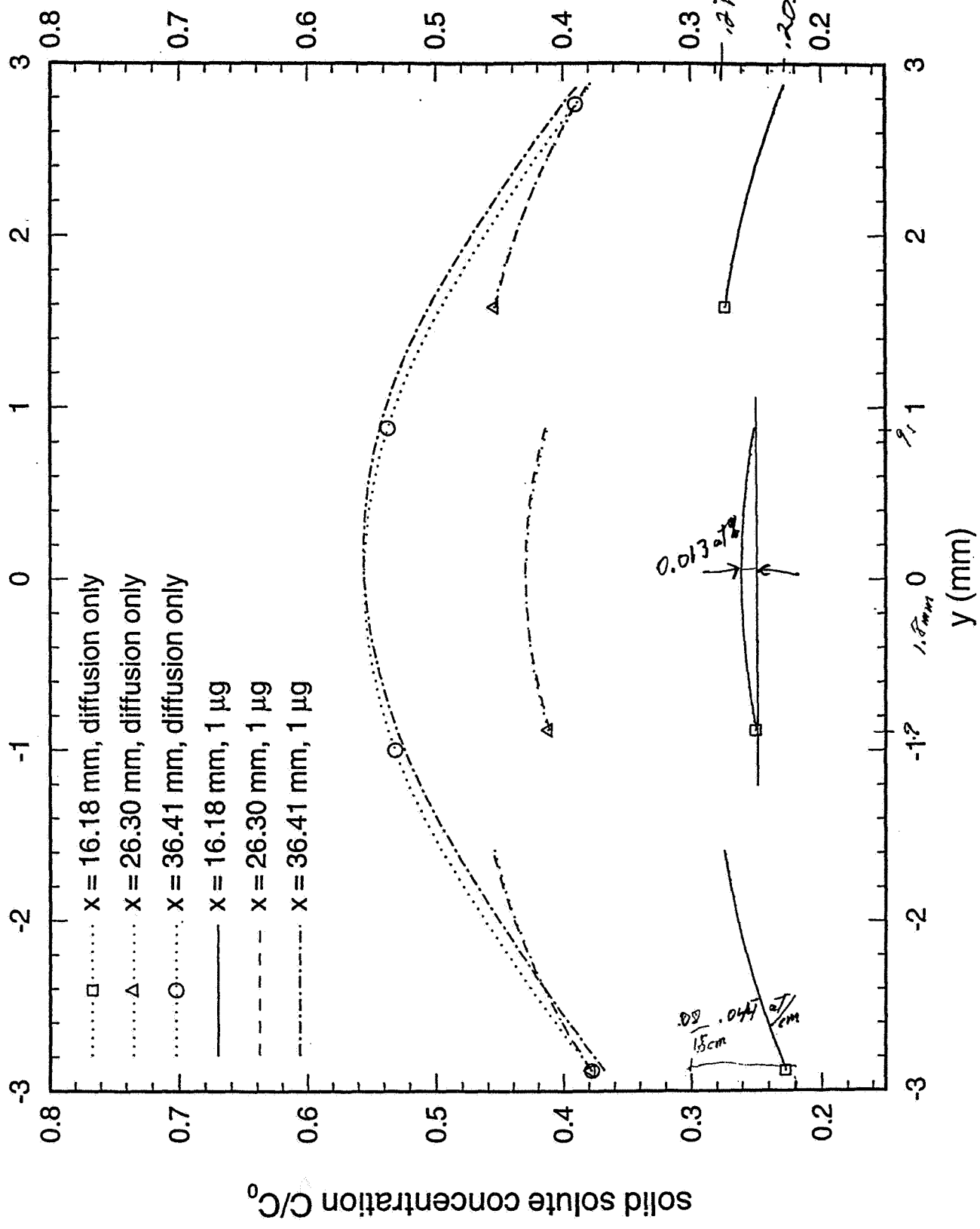


Figure 6. Simultaneous

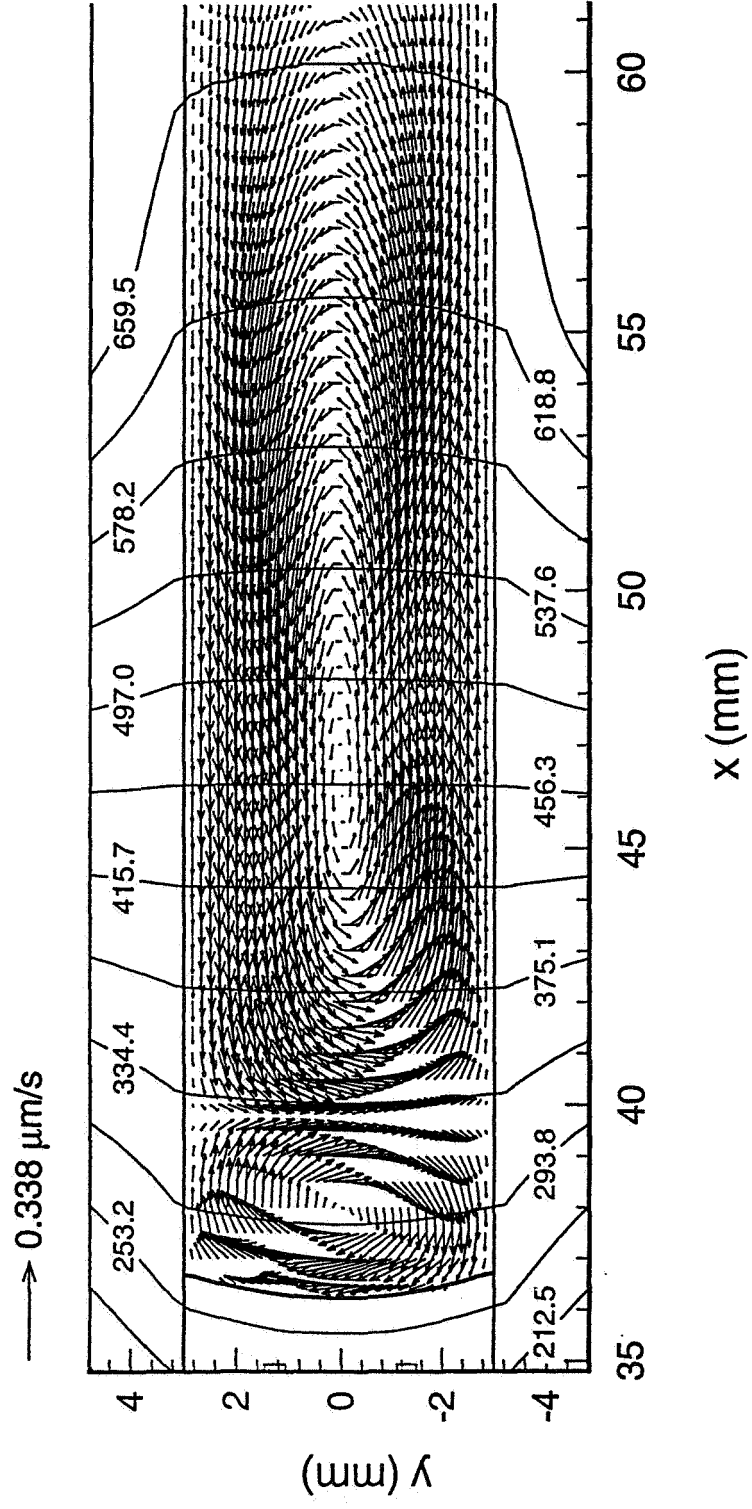
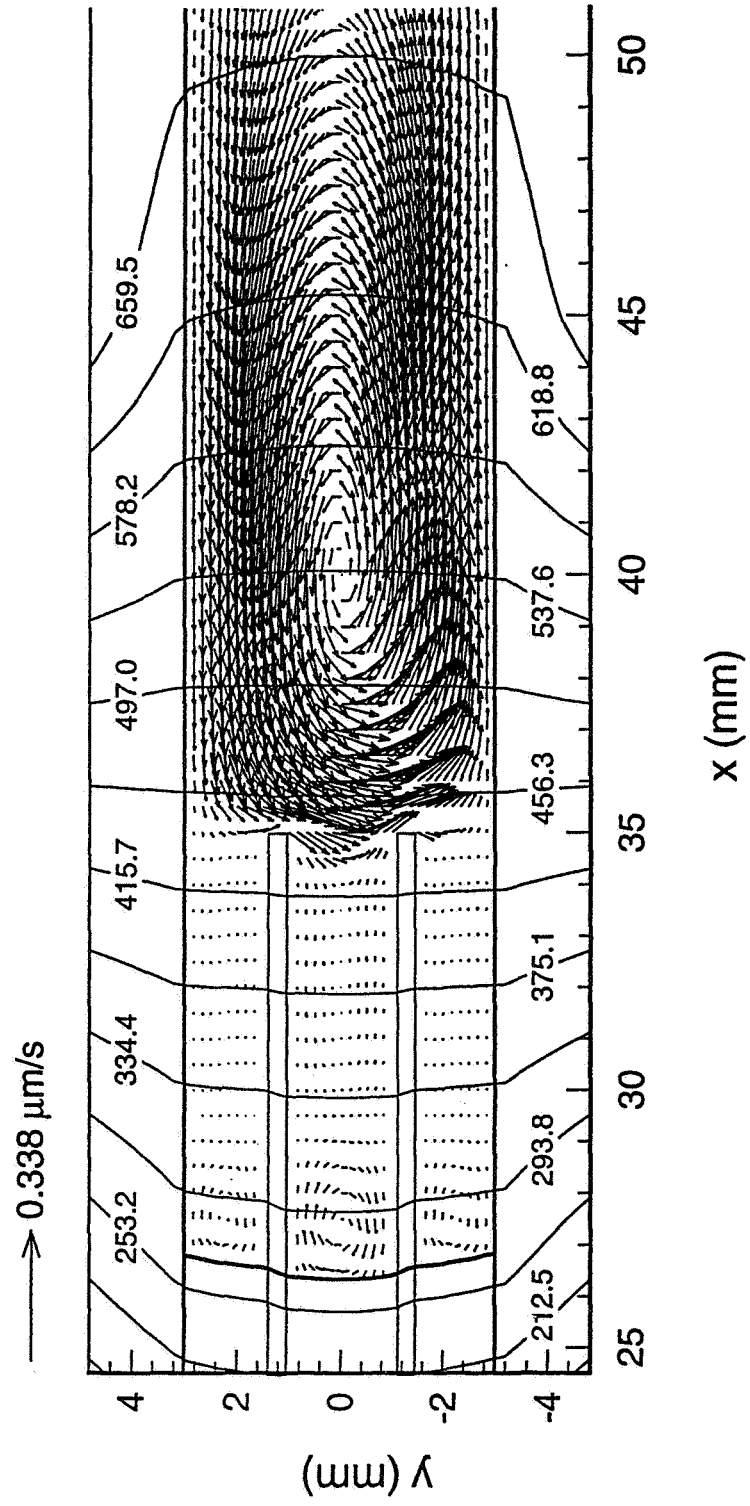
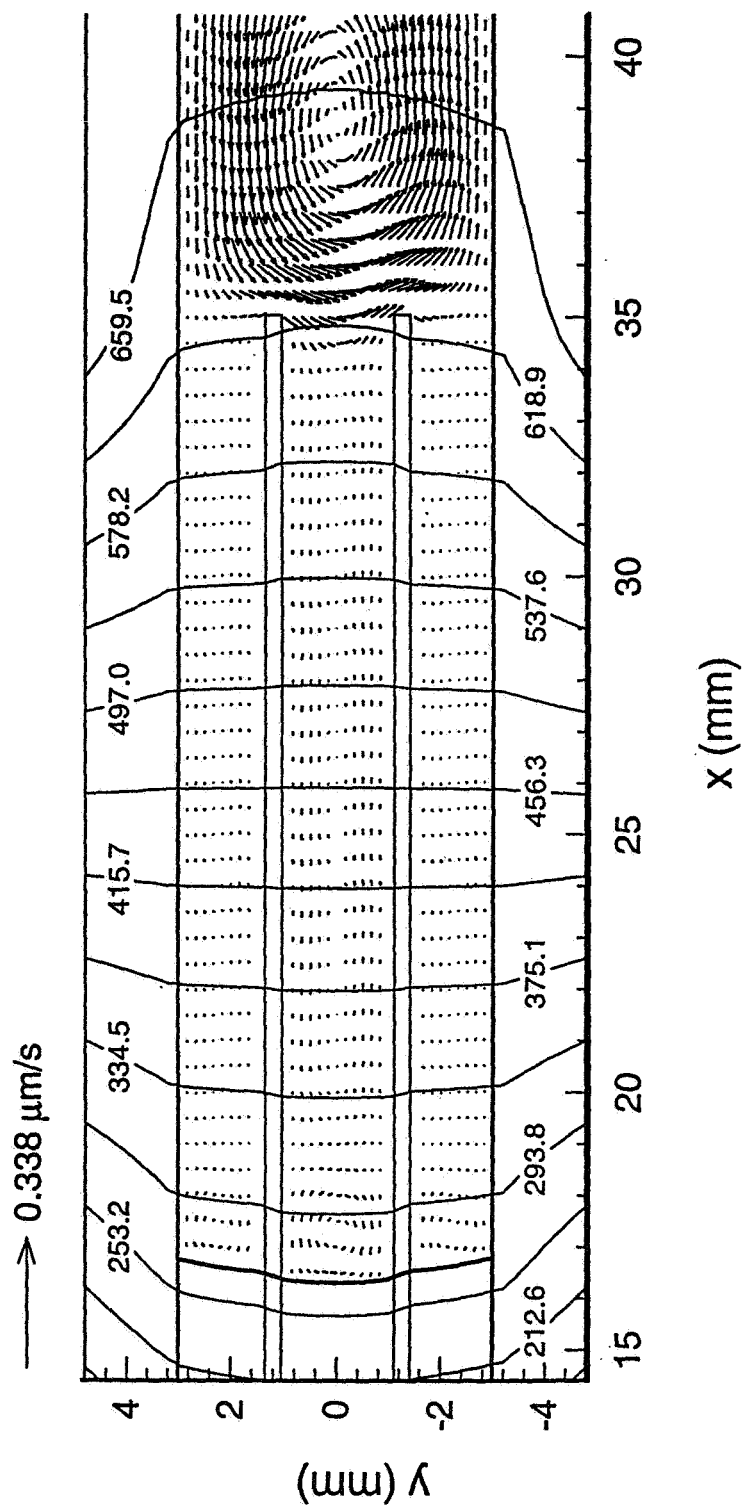


Figure 5(c). Simonsen et al.



(b)-

Figure 5(b), Simpson et al.



(a)

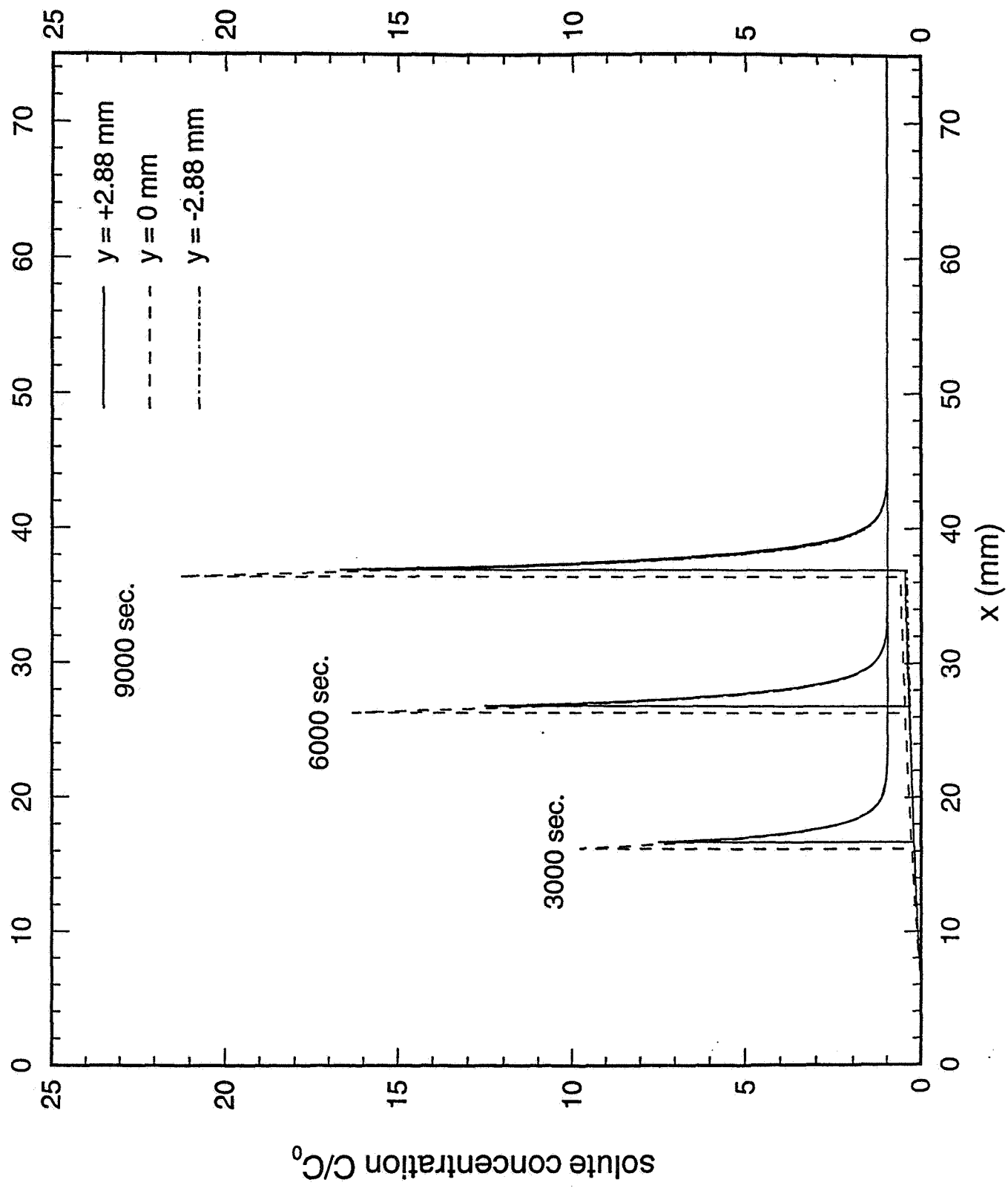
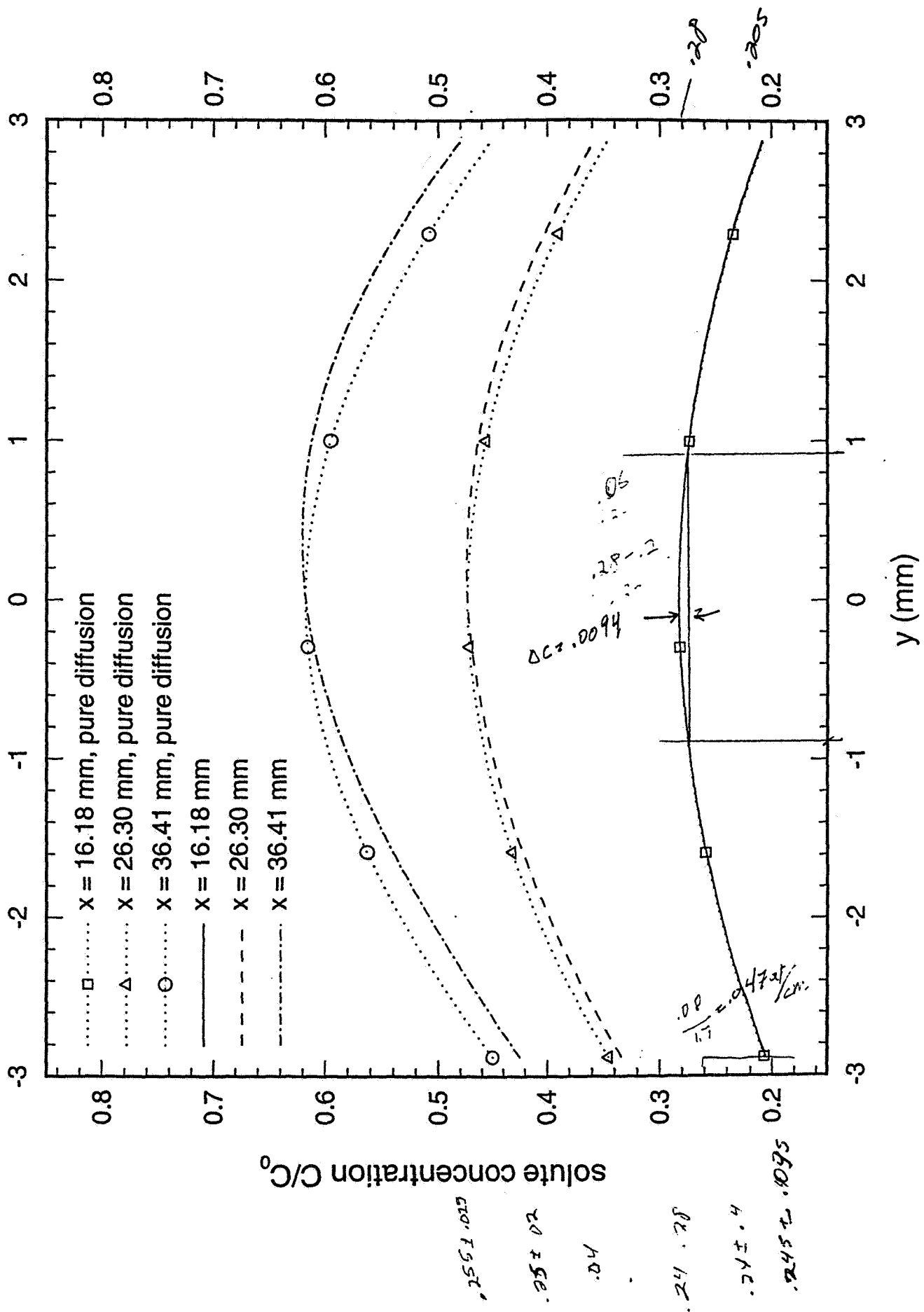
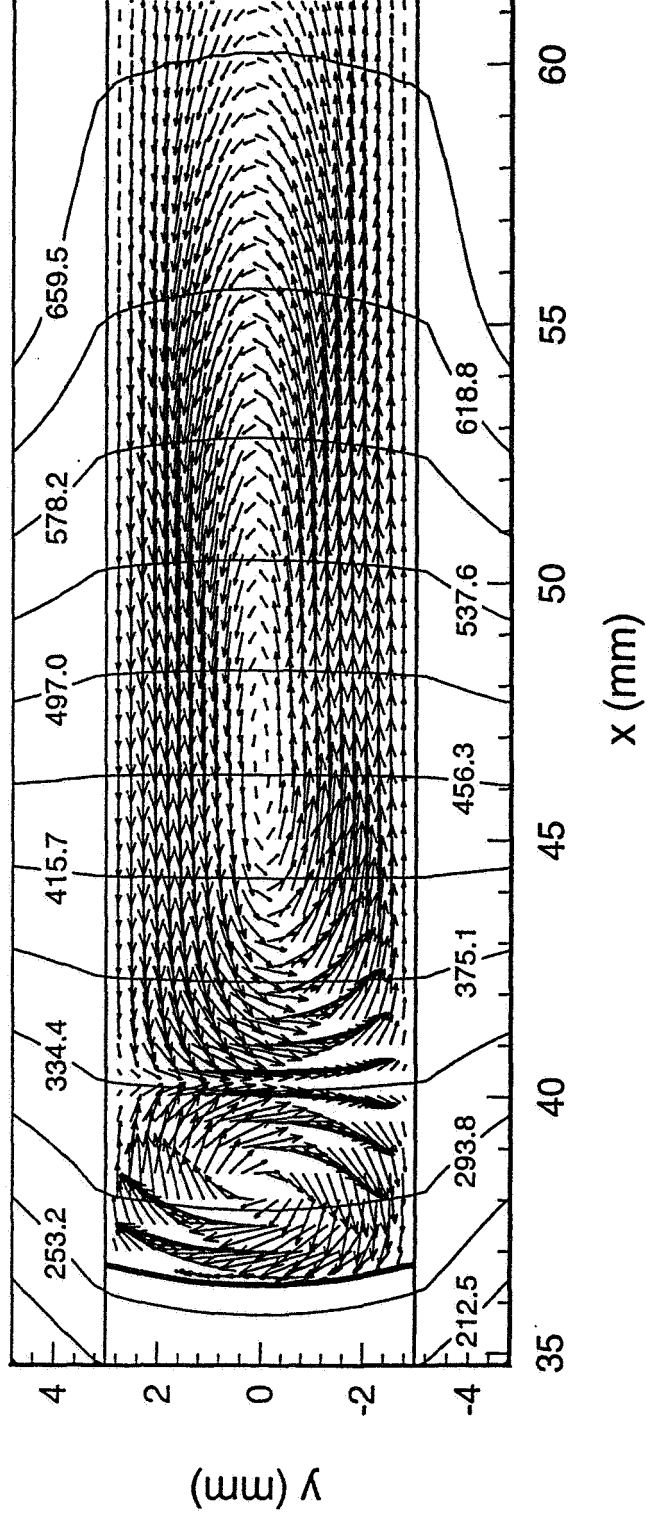


Figure 4. Solute concentration



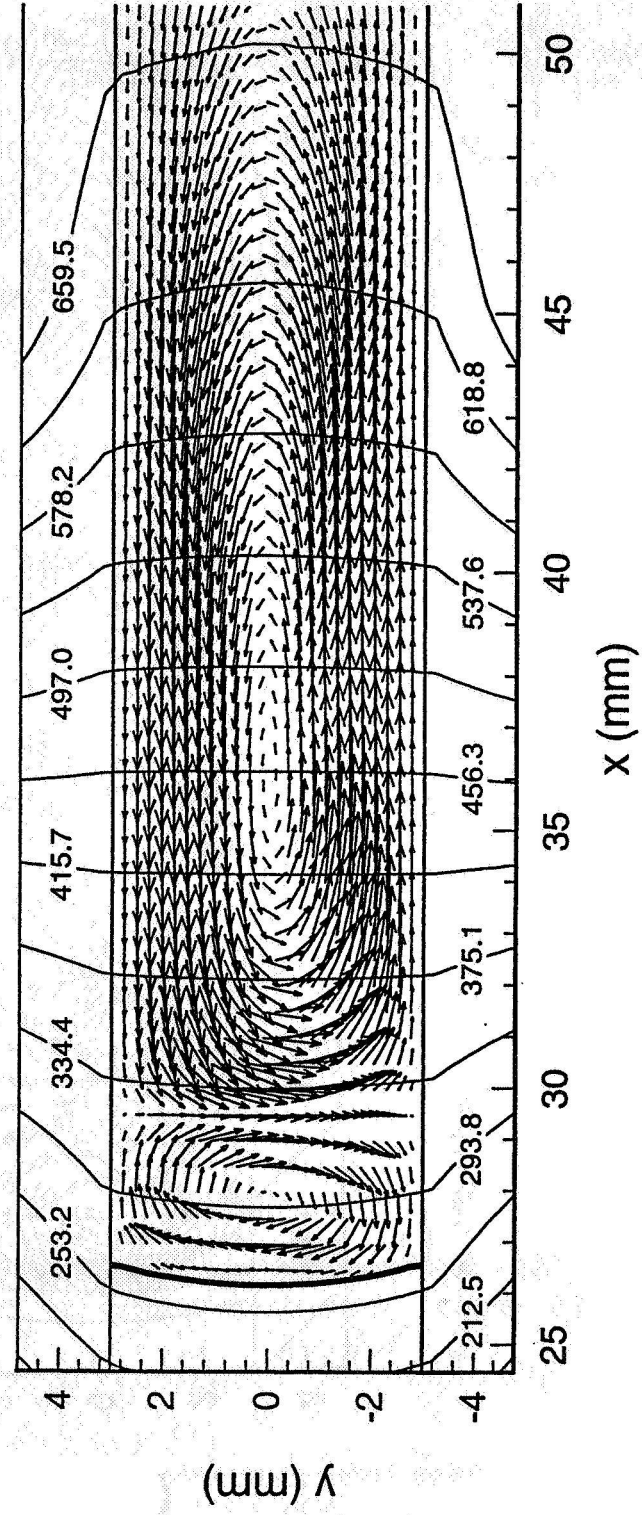
→ 0.338 $\mu\text{m/s}$



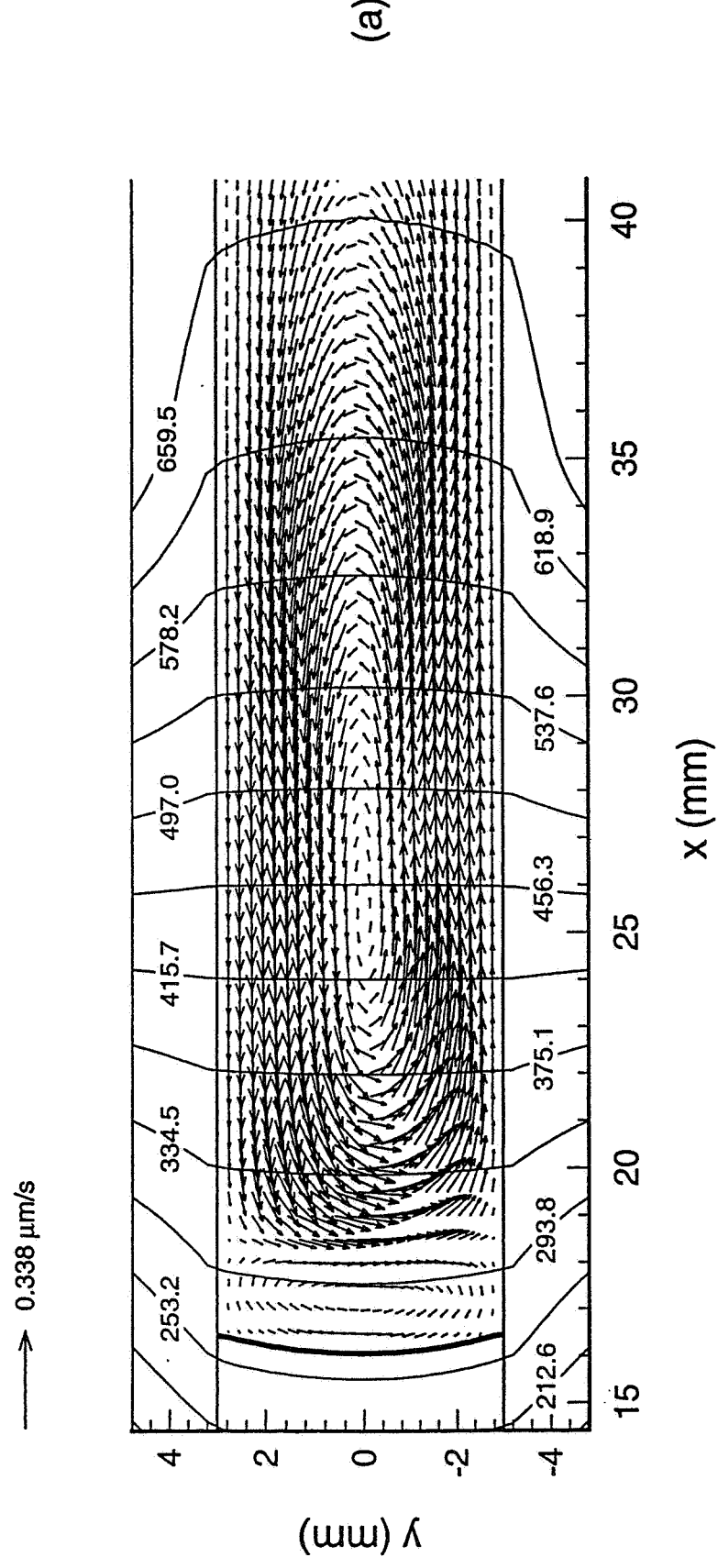
(c)

Figure 2(c), Simpson et al., 2000

→ 0.338 $\mu\text{m/s}$



(b)



(a)

Figure 2(a), Simpson et al.

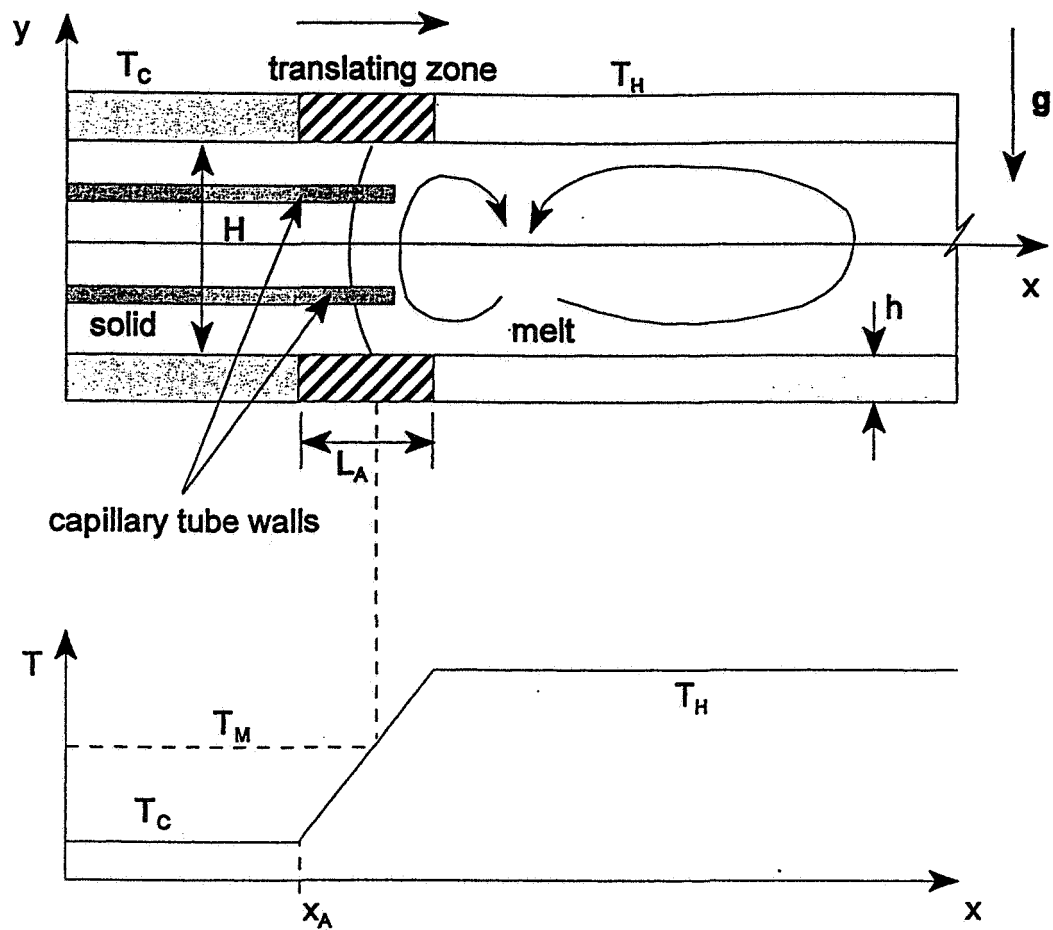


Figure 1, Simpson et al.

Figure Captions

Fig. 1. Schematic of the Bridgman crystal growth process and furnace temperature profile.

Fig. 2. Velocity vectors and isotherms for the Bridgman growth of Bi-1.0 at.% Sn **without** the capillary at (a) 3,000 (b) 6,000 and (c) 9,000 s. The thick solid line indicates the location of the solid/liquid interface. The velocity vectors are shown at every other location in the x-direction. A primary counter-clockwise convective cell is evident in all three panels. A secondary clockwise cell, driven by solutal gradients, develops with time.

Fig. 3. Traces of solute concentration across the solidified material at various x-locations for Bi-1.0 at.% Sn, **without** the capillary tube in the domain. The dotted lines correspond to diffusion only (no convection) results.

Fig. 4. Longitudinal solute concentration traces at three different y-locations for Bi-1.0 at.% Sn, no capillary.

Fig. 5. Velocity vectors and isotherms for the Bridgman growth of Bi-1.0 at.% Sn **with** the capillary at (a) 3,000 (b) 6,000 and (c) 9,000 s. The thick solid line indicates the location of the solid/liquid interface. The velocity vectors are shown at every other location in the x-direction. The horizontal bars extending to $x \approx 35$ mm are the walls of the capillary tube. Convective levels are significantly smaller than those indicated in Fig. 2. *There is a clockwise flow cell near the interface with a maximum $V = 7 \text{ in/s}$, $V = 1 \text{ in/s}$.*

Fig. 6. Traces of solute concentration across the solidified material at various x-locations for Bi-1.0 at.% Sn, **with** the capillary tube in the domain. The dotted lines correspond to diffusion only (no convection) results.

Fig. 7. (a) Longitudinal solute concentration traces at three different y-locations for Bi-1.0 at.% Sn, with capillary and (b) magnified view showing the longitudinal segregation caused by the area effect of the capillary.

in microgravity, *Heat Transfer* 1998, Vol. 7, pp. 241-246.

Timchenko, V., Leonardi, E. and de Vahl Davis, G., 1997, FRECON3V User's Manual, University of New South Wales, School of Mechanical and Manufacturing Engineering, Report 1997/FMT/1, and FRECON3V Programmer's Manual, Report 1997/FMT/2.

Yao, M. and de Groh III, H. C., 1993, Three-dimensional finite element method simulation of Bridgman crystal growth and comparison with experiments, *Num. Heat Transfer, Part A*, Vol. 24, pp. 393-412.

Yao, M., de Groh III, H. C. and Abbaschian, R., 1997, Numerical modeling of solidification in space with MEPHISTO-4 (Part 1), *35th Aerospace Sciences Meeting and Exhibit*, Reno, NV, Paper AIAA 97-0449.

Yao, M., Raman, R. and de Groh III, H. C., 1995, Numerical simulation of heat and mass transport during space crystal growth with MEPHISTO, NASA Technical Memorandum 107015.